Proceedings of the 4th International Conference on Computing Innovation and Applied Physics
DOI: 10.54254/2753-8818/83/2025.20179

Windblown Leafs: Drag Reduction Through Shape Reconstruction in Thin Foldable Plates

Zihan Zeng[1,a,*]

[1]*Zeng Zihan, Chongqing Nankai Secondary School, Chongqing, China*
a. r18623349949@163.com
**corresponding author*

Abstract: The physical mechanism of drag reduction through shape reconstruction in a flow field has been extensively studied in geometries primarily modeled as bending deformable plates and beams. Leaves, consisting mainly of blades and veins, represent a typical thin-walled structure, where the thin-walled nature of the veins can result in significant deformation under fluid loading. Unlike rigid structures, leaves in a flow field can achieve drag reduction through shape reconstruction, thereby resisting damage. The deformation of leaves reduces the drag acting on their structure until the fluid loading reaches an upper limit and no longer increases with flow speed. Additionally, the presence of hinge-like structures on thin sheets results in varying degrees of bending along specific degrees of freedom. We observe a development trend in the study of passive deformation of flexible bodies: from simple two-dimensional flexible fiber deformation to three-dimensional flexible thin plate deformation; from deformation of plates with uniform stiffness to those with non-uniform stiffness distribution. The idea of pre-setting creases on thin plates is inspired by the veins of leaves. This controllable deformation mode concentrates motion along the creases, functioning like hinges around which the surfaces rotate. The crease pattern provides conditions for three-dimensional deformation, allowing shape changes along specific folding paths. Inspired by this, we explore the fluid-flexible body coupling process of this flexible thin plate deformation and verify numerical simulation results in wind tunnel experiments. We conduct studies on shape reconstruction and drag characteristics of flexible thin plates with different stiffness and geometries in wind fields, investigating the mechanisms of shape reconstruction, principles of drag reduction, and the influence of vein distribution on the drag reduction effect.

Keywords: Shape reconstruction, Drag reduction, Fluid-structure interaction, Flexible thin plates, Leaf-inspired structures.

1. Introduction

1.1. Research Background and Significance

Flexible bodies in flow fields can bend, twist, or stretch, and this ability to self-reconstruct is crucial in studying the biomechanics of organisms in strong winds or currents. Tree leafs (referring to monocots' leaf structure, in this case), are A monocot leaf typically consists of a blade (or lamina, the flat part characterized by its long, narrow shape and parallel venation), sheath (the base of the leaf

© 2025 The Authors. This is an open access article distributed under the terms of the Creative Commons Attribution License 4.0 (https://creativecommons.org/licenses/by/4.0/).

DOI: 10.54254/2753-8818/83/2025.20179

that wraps around the stem, providing structural support), and often a ligule (a small membranous or hairy structure, is located at the junction where the blade meets the sheath). Compared to rigid structures, flexible leaves significantly reduce the loads they bear, thus reducing the risk of breaking to some extent. Early studies on the physical mechanisms of shape reconstruction of flexible thin plates mainly focused on deformation under non-fluid forces. Chaieb and Melo experimentally studied the formation process and physical mechanism of variable cones. Cerda and Mahadevan discussed the conical surfaces and crescent-shaped singularities of wrinkled sheets. Cerda et al. experimentally observed gravity-induced wrinkling of flexible thin circular plates and analyzed the formation of a series of deformation modes. Schouveiler and Eloy studied flow-induced wrinkling of flexible thin circular plates through water tunnel experiments, proposing the Cauchy number as a control parameter based on the number of circumferential wrinkles formed due to circular plate deformation.



Figure 1: Leaf structure of a typical beech leaf. Shoot by cocoparisienne, photo source: https://pixabay.com/photos/beech-beech-leaf-beech-leaves-754156/

To explore the drag reduction mechanism, the final flow state of the fluid-structure coupling system needs to be analyzed. Numerous experiments and numerical simulations have been conducted on flow around rigid thin plates. Shenoy and Kleinstreuer conducted numerical studies on flow around thin circular plates, distinguishing different steady and unsteady wake modes based on Reynolds number (Re).

For real leaves, Vogel was the first to study deformation-induced drag reduction in broad-leaved plants under strong winds, discovering that leaves bend and curl into "U" or conical shapes as wind speed increases, significantly affecting drag. Vogel found that the drag coefficient of leaves and wind speed are exponentially related, with α known as the Vogel index, representing the difference between deformed leaves and rigid blunt bodies and indicating the leaf's deformation capability. Shao Chuanping and colleagues from China Jiliang University conducted extensive wind tunnel experiments on leaf drag characteristics, such as fixing a single tulip tree leaf vertically and conducting wind tunnel tests. As wind speed increased, the petiole bent, and the drag coefficient decreased, stabilizing around 0.1 when the leaf curled into a conical shape, with the Vogel index α approaching 0, indicating a drag limit at certain wind speeds.

DOI: 10.54254/2753-8818/83/2025.20179

2. Theoretical Model Analysis

In the initial stage of leaf deformation in a wind field, air flow exerts pressure on the leaf surface. According to Bernoulli's principle, pressure is higher on the windward side and lower on the leeward side; uneven pressure distribution causes initial deformation. The deformation changes the airflow path, altering the leaf's windward area and shape, affecting local flow velocity and pressure distribution, and thereby reducing drag. Over time, leaves reach a stable deformed shape under wind force and elastic force, reducing vortices and separation zones, further decreasing drag. Based on our daily observations, the leaf blades fold along the vein. Vein structure undertakes the highest amount of stress -- which is also where the most significant deformation takes place -- helps control flow separation points and distribute load. Observations also suggest that the interaction of fluid load and elastic recovery force causes deformation, driving us to introduce Cauchy number to compare the effects of fluid load and elastic force, where higher values indicate higher extent of deformation.

$$C_y = \frac{\rho U^2 R^2}{\kappa} \tag{1}$$

For incompressible steady flow, Navier-Stokes equations describe fluid motion:

$$\rho(\frac{\partial u}{\partial t} + (u \cdot \nabla)u) + \nabla p - \mu\nabla^2 - f = 0 \tag{2}$$

where ρ is density of air, u is the fluid velocity vector, p is air pressure, μ is dynamic viscosity, and f is body force.

2.1. Establishing 2D Conical Model

Observing the PVC bionic leaf bending in experiments, let us simplify our folding model this way: several rigid surfaces resemble the leaf blades, and the veins are represented by hinges with torsional stiffness. In a 2D circumstance, we first analyze the force and energy conditions of two plates folding around a single crease in a uniform flow field with wind speed U. This approach has several benefits: 1) leaf deformation is simply and visually quantified by the opening angle change from initial θ_0 to θ; 2) study on the 2D folding mechanism can be generalized to the 3D symmetrical leaf model in our research. The crease's elastic potential energy of the deformed plate per unit length can then be written as: $E_{el} = \frac{1}{2}\kappa(2\theta - 2\theta_0)^2$. Based on the Second Law of Thermodynamics, when the plate and fluid reaches equilibrium, the system reaches a minimum energy state ($E_{el} - WD = min$), where WD is the work done by the fluid. Relatively high Reynolds number is observed throughout the experiments, suggesting that shape drag dominates over friction drag, in which the former is given by $F_{PD} = \frac{1}{2}\rho U^2 C_D A$, where C_D is the drag coefficient. Furthermore, the post-folding model shapes like a wedge, which helps us draw distinction between different layers of air: that far away from the structure (inertia-dominated, where pressure is rationally approximated as constant), near the cone structure (affected by viscosity, characterized using Falkner-Skan boundary layer flow equations for pressure distribution around the angular discontinuity). Recognizing that velocity increases exponentially in the boundary layer theory, we first write down the wind velocity passing arbitrary position x as: $u_e(x) = (\frac{x}{R})^2 U$; The differential pressure equation is then given by Bernoulli's equation: $P(x) + \frac{1}{2}\rho u_e(x)^2 - \frac{1}{2}\rho U^2 = 0$, leading us to write:

$$P(x) = \frac{1}{2}\rho U^2 - \frac{1}{2}\rho u_e(x)^2 = \frac{\rho U^2}{2}(1 - (\frac{x}{R})^{\frac{2\theta}{\pi-\theta}}) \tag{3}$$

Substituting $P(x)$ in expression for work done on the facet WD:

DOI: 10.54254/2753-8818/83/2025.20179

$$E_{el} - WD = \frac{1}{2}\kappa(2\theta - 2\theta_0)^2 - 2\int_{\theta_0}^{\theta}(\int_0^R P(x)xdx)d\theta \tag{4}$$

$$E_{el} - WD = \frac{1}{2}[\kappa(2\theta - 2\theta_0)^2 + \rho U^2 R^2 \int_{\theta_0}^{\theta}(\frac{\theta}{\pi})d\theta] \tag{5}$$

when $(E_{el} - WD)$ reaches a minimum, $\frac{d(E_{el}-WD)_\theta}{d\theta} = 0$, thus the corresponding equilibrium angle is characterized by:

$$\theta(1 + \frac{C_y}{8\pi} - \frac{\theta_0}{\theta}) = 0, C_y = \frac{\rho U^2 R^2}{\kappa} \tag{6}$$

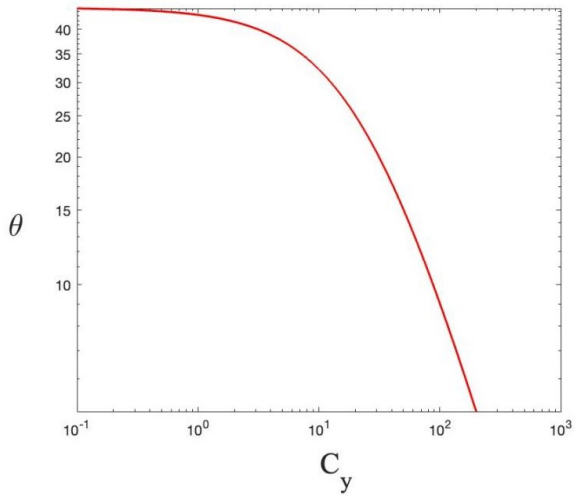

Figure 2: Deformation angle - Cauchy number relationship

This allows us to write down the mathematical expression relating equilibrium angle and different Cauchy Numbers, as well as change in drag force for increasing Cauchy Number. Then, compute the drag force as integral of pressure acted on the surface $F_{PD} = 2\int_0^R P(x)sin\theta dx$, given pressure: $P = \rho U^2 sin^2\theta$.

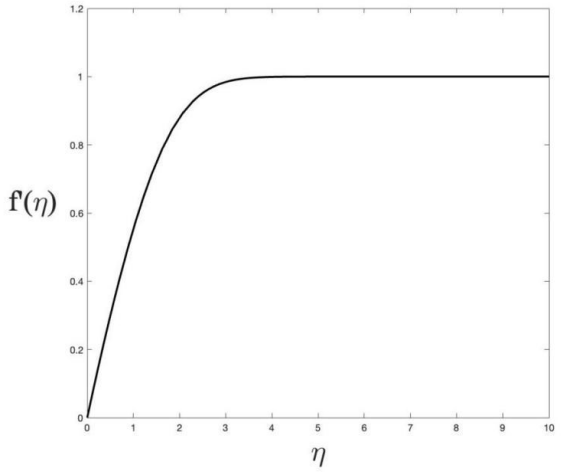

Figure 3: Pressure-induced drag - Cauchy number relationship

DOI: 10.54254/2753-8818/83/2025.20179

2.2. Three-Dimensional Geometric Model for Folding and Its Mechanism

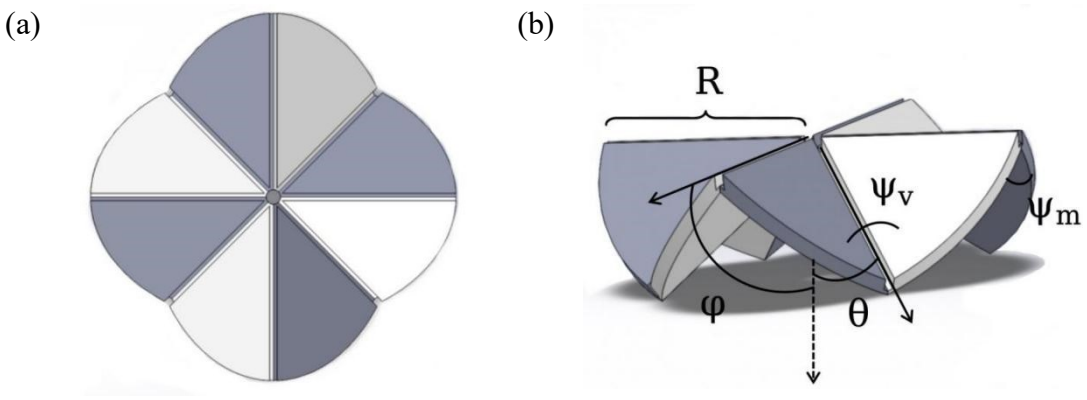

Figure 4: Scheme of the geometry of the example 8-crease bionic structure modeled with SOLIDWORKS, displaying the crease pattern (a) from the front (b) from the side, and the related parameters needed for discussion afterwards

First, in our configuration we assume that all motions are concentrated at the hinges connecting the rigid surfaces. It contains an even number of N creases, which can then be divided into N/2 mountain creases and N/2 valley creases, with each two creases separated by angle $\alpha = 2\pi/N$. Having a symmetrical folding model allows us to analyze kinematics with 1 degree of freedom (DOF), thus only one variable is needed to describe the process, which we choose as angle θ separating a fold and the central supporting axis. Brunck *et al.* (2016) provided alternative methodology allowing us to circumvent the lack of an explicit expression of the geometrical constraints in this context in terms of space angle of folding φ: by characterizing deformation with vectors instead of angles, we can render the energy minimization straightforward. Following the approach, we write down the geometric constraints - the relationship between θ and φ:

$$cos\theta cos\varphi - cos\alpha(1 - sin\theta sin\varphi) = 0 \tag{7}$$

it is then rewritten as:

$$\varphi(\theta) = \begin{cases} arccos(\frac{cos\alpha cos\theta}{1+sin\theta sin\alpha}), for\ 0 \le \theta \le \pi/2 \\ arc(\frac{cos\alpha cos\theta}{1-sin\theta sin\alpha}), for\ \pi/2 < \theta \le \pi - \alpha \end{cases} \tag{8}$$

Since the present study reminds us that the deformation happens within the region $0 \le \theta \le \pi/2$, we will constrict any operation to this range in the following content. Looking back to the analysis, we can easily yield the windward area (that is, the area projected in the xy plane):

$$A = \pi R^2 sin\theta sin\varphi \tag{9}$$

2.3. Skin Drag-Affected Motion

Then, we seek to study the sheer stress acted on the wall based on Falkner-Skan solution of boundary flow. Consider first the precise global interpretation involving the flow past a symmetric wedge. It transpires that this steady potential flow has a surface velocity U. On the side, the half-angle of folding, that is, $\frac{1}{2}$ the angle of the wedge, gives m given that $\theta = \frac{2m}{m+1}$. Taking zero velocity at the wall, the pressure gradient along the positive horizontal direction can be derived from the Bernoulli's equation:

DOI: 10.54254/2753-8818/83/2025.20179

$-\frac{1}{\rho}\frac{\partial P}{\partial x} = u_e\frac{du_e}{dx} = (\frac{x}{R})^2 U\frac{d[(\frac{x}{R})^2 U]}{dx}$, at the boundary layer. Combining the boundary layer equations and the stream function, we first yield the single governing equation:

$$\frac{\partial\psi}{\partial n}\frac{\partial^2\psi}{\partial x\partial n} - \frac{\partial\psi}{\partial x}\frac{\partial^2\psi}{\partial^2 n} = mC^2x^{2m-1} + \gamma\frac{\partial^3\psi}{\partial n^3} \tag{10}$$

The first step to solving this equation is to recognize the similarity variable, η, with brevity by anticipating that it is the same as for the Blasius solution except that U is now a function of x:

$$\eta = n(\frac{U}{4\nu x})^{\frac{1}{2}} = n(\frac{Cx^{m-1}}{4\nu})^{\frac{1}{2}} \tag{11}$$

Similarly, the solution given by the stream function is then written as:

$$\Psi = (4\nu Ux)^{\frac{1}{2}}F(\eta) = (4\nu Cx^{m+1})^{\frac{1}{2}}F(\eta) \tag{12}$$

$$\frac{u}{U} = \frac{dF(\eta)}{d\eta} \tag{13}$$

$$2(\mathrm{m}+1)\mathrm{F}\frac{\mathrm{d}^2\mathrm{F}}{\mathrm{d}\eta^2} + \frac{\mathrm{d}^3\mathrm{F}}{\mathrm{d}\eta^3} + 4\mathrm{m} - 4\mathrm{m}(\frac{\mathrm{dF}}{\mathrm{d}\eta})^2 = 0 \tag{14}$$

Given the boundary conditions: $\mathrm{v} = 0$ on the solid surface, $\eta = 0$, and $(dF/d\eta)_{\eta=0}$, accordingly. Both methodologies satisfy the Falkner-Skan equation:

$$f''' + ff'' + \frac{2m}{m+1}(1 - f'^2) = 0, m = \frac{\theta}{\pi-\theta} \tag{15}$$

This can be solved numerically, and its solution and derivatives give the velocity field and value of shear stress acting on the plates:

$$\tau(x) = \rho\upsilon(\frac{\partial v}{\partial y})_{y=0} = \rho\sqrt{\upsilon U^3(m+1)x^{3m-1}/2R^{3m}}f''(0) \tag{16}$$

in which υ denotes the constant of kinematic viscosity, and the shear stress induces no torque on the fold (since the friction induced by it is tangential to the plates), meaning that it does not contribute to the formation of the equilibrium shape. The total skin drag $\mathrm{F_{SD}} = 2\int_0^{\mathrm{R}}\tau(\mathrm{x})\mathrm{dx}\cos\theta$, to which the shear stress we recognized does contribute, is rewritten in a dimensionless form in order to yield patterned correlations afterwards: $\overline{\mathrm{F_{SD}}} = \frac{\mathrm{F_D}}{\kappa} = \frac{2\sqrt{2(\mathrm{m}+1)}}{3\mathrm{m}+1}\frac{\mathrm{C_y}}{\sqrt{\mathrm{Re}}}\mathrm{f}''(0)\cos\theta$, $\mathrm{Re} = \mathrm{UR}/\upsilon$. In the previous models under inviscid flow, drag is characterized by Cauchy number $C_y = \frac{\rho U^2R^2}{\kappa}$ which is only dependent of the field velocity and model size; in the viscid case, Reynolds number is introduced, rectifying the drag-Cauchy number correlation. Rewriting the drag distribution with correction, Reynolds number can be denote as a function of $\mathrm{C_y}$ since $\mathrm{U} = \sqrt{\kappa\mathrm{C_y}/\rho\mathrm{R}^2}$. The figure below illustrates all drag-Cauchy number relation: $\overline{\mathrm{F_{PD}}} - \mathrm{C_y}$, $\overline{\mathrm{F_{SD}}} - \mathrm{C_y}$, and the total drag $\overline{\mathrm{F_D}} = \overline{\mathrm{F_{PD}}} + \overline{\mathrm{F_{SD}}}$. Observing the graph, pressure-induced drag contributes more to the total drag than does skin drag, which is approximately one order of magnitude smaller in the low-$\mathrm{C_y}$ region ($10^{-2} < \mathrm{C_y} < 10^1$) than the latter; while when entering the high-$\mathrm{C_y}$ region ($\mathrm{C_y} > 10^1$) where the momentum-induced drag $\overline{\mathrm{F_{PD}}}$ experiences a decay, skin drag plays a role as the plates have a tendency to align with the flow, leading to a plateau and an afterward re-rise of the total drag. This plateau corresponds with the one observed in our experiment, and can thus be concluded to be caused by the act of skin drag $\mathrm{F_{SD}}$.

DOI: 10.54254/2753-8818/83/2025.20179

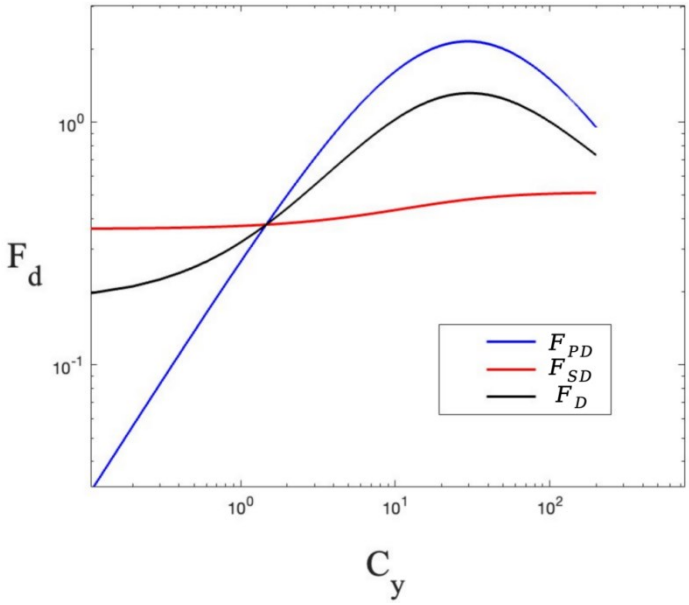

Figure 5: Inertia-induced drag force, viscosity-caused skin drag and the resultant drag force acted on the plates as a function of Cauchy number

3. Experimental Research

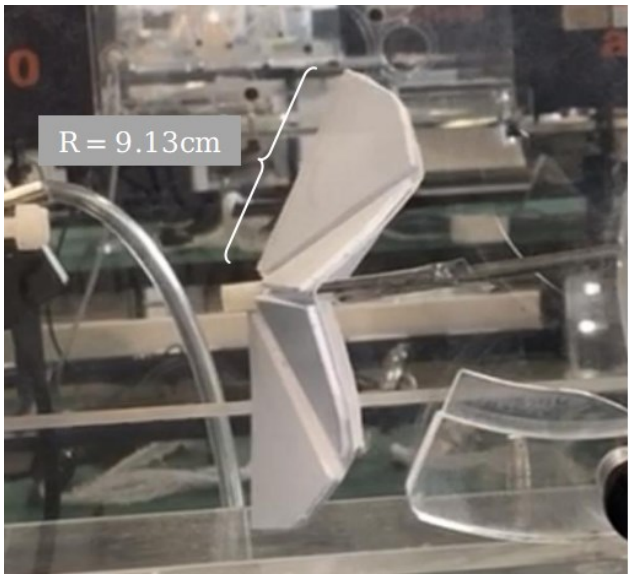

Figure 6: Side view of the structure at initial folding stage in experiment. The radius of both plates is 9.13cm, a constant crucial in identifying the characteristic radius in expression of Reynolds number, $\mathrm{Re} = \mathrm{UR}^*/\nu$.

3.1. Experimental Setup and Materials

We use a Armfield C 15-10 small wind tunnel to generate uniform wind field. The configuration is supported by a steel rod fixed to the left wall of the tunnel which, we assume, presents negligible effect on the uniformity of wind velocity and pressure. The materials used for fabricating the circular plates are glossy photo paper for creases and polyvinyl chloride (PVC) for blades. The PVC blades are cut into fan shape using laser, and the shape of photo paper is cut with scissor. The camera setup

DOI: 10.54254/2753-8818/83/2025.20179

includes: GoPro sport camera for filming the frontal view inside the wind field, and a regular phone to record the evolution of folding from the side.

3.2. Pre-Experiment Procedure

3.2.1. Fabricate configuration

We stick two layers of different materials with different thicknesses (19.3mm thick PVC scalloped plates as blades and 0.14mm thick circular glossy photo paper as veins, or creases, connecting the blades) together to construct our bionic leaf model. In the selection of materials, we make sure that the blade sections remain relatively rigid and the deformation is concentrated at the creases; furthermore, one advantage of using photo paper as the bottom layer is that it is not only thin enough so that we can assume its mass is negligible, but also it is more resistant to plastic deformation than regular paper. Note that we use seccotine to stick the planes together so that any slippage can be neglected in our study of mechanical response.

(a)  (b) 

Figure 7: Measurement of the thickness of the (a) plate and (b) crease

3.2.2. Test experimental parameters

The parameters we seek to test include: the mechanical response of deformation featured by the stiffness of creases (related to base layer thickness, 0.14mm), number of creases N (8 and 12), and the incoming wind speed U (ranging from 8m/s to 15m/s) and the corresponding Reynolds numbers (Re).

Measurement of torsional stiffness κ

To test the mechanical response of folding, we first fabricate a single crease, denoted by a torsional hinge with torsional stiffness, $\kappa = T/\theta$, a constant relating the flow applied-torque and the angular deformation $\psi - \psi_0$, written as $T = \kappa W(\psi - \psi_0)$, where W is the width of the crease. Second, we attach one facet to a vertical support and hook a weight beam at the bottom of the other facet. With this equation, the value κ can be calculated after measuring the angle of folding, $|\psi - \psi_0|$ as we gradually increase the pulling force at the bottom facet. From the $|\psi - \psi_0| - T$ data, we observe an expected linear relationship, with slope denoting $1/\kappa W$.

However, due to

DOI: 10.54254/2753-8818/83/2025.20179

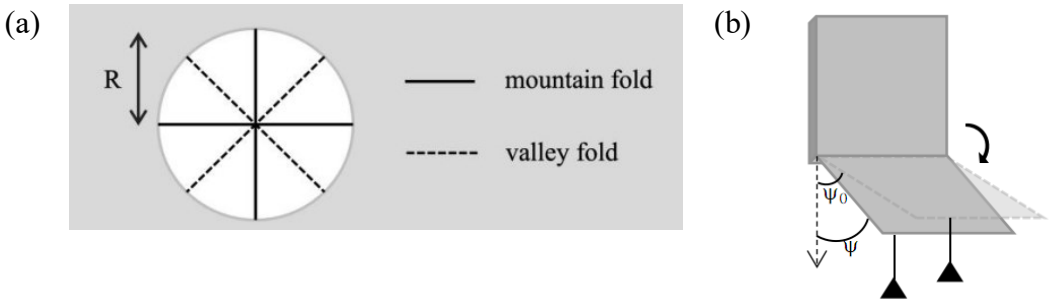

Figure 8: (a) Fold pattern of an 8-crease (b) Set up of measuring the fold stiffness

Reynolds number Re

The Reynolds number $Re = UR^*/\upsilon$ (where U is the velocity of field flow, R is the characteristic radius of windward facet, and υ represents the air viscosity) is dependent of the size of the cell R, and it ranges from 10^3 to 10^5 in our study (taking plate radius $R = 9.13cm$, $\upsilon = 1.5 \times 10^{-5} m/s^2$, and U ranging from $5m/s$ to $15m/s$, when the cell lays parallel to the y-axis). Values of Re is computed in the figure below for varying input flow velocity, and no obvious difference of order of magnitude is observed.

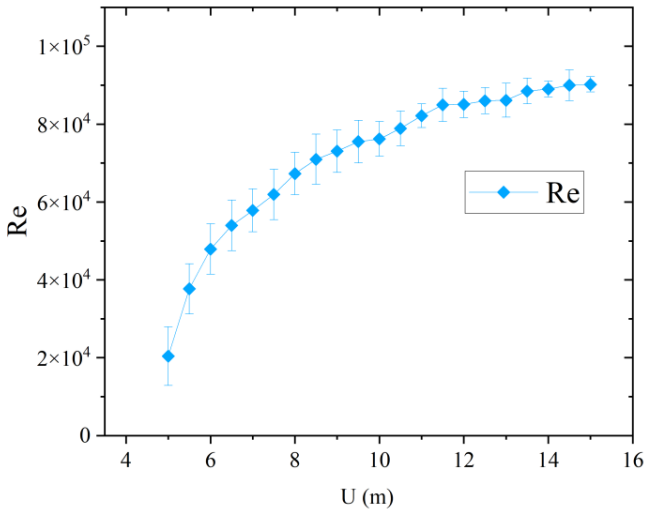

Figure 9: Measurement of Reynolds number for varying flow speed. At different flow speed, the windward area of the plate varies, affecting the characteristic radius.

3.3. Wind Tunnel Experiment

Now we place the bionic plate in front of wind tunnel, and fix front and side cameras; start the wind tunnel, gradually increase wind speed, record steady deformation state at each speed (the wind speed is initialized at 5m/s, and for every 0.5m/s increase, we maintain the speed for 2 seconds and record the angular deformation at the end of the 2s-period). The process is repeated 5 times with five different plate for each set in order to eliminate the effect of elastic deformation at the central hole.

DOI: 10.54254/2753-8818/83/2025.20179

(a) (b)

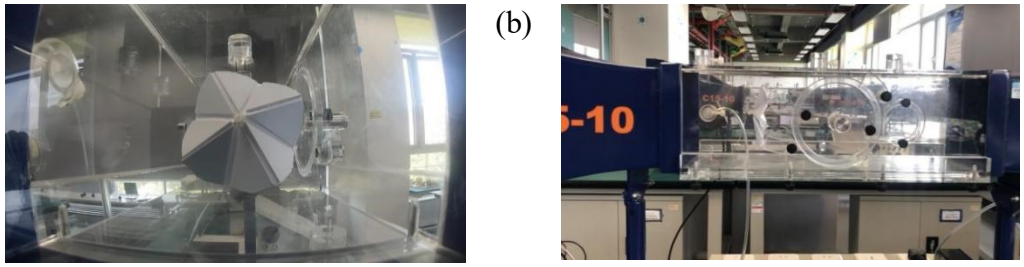

Figure 10: The 8-crease configuration in the wind tunnel from the (a) frontal perspective (b) side perspective

Four specimens are then studied, ranging the fold stiffness $\kappa = 10^{-3}\sim10^{-2}$, and the number of creases $N = 8, 12$.

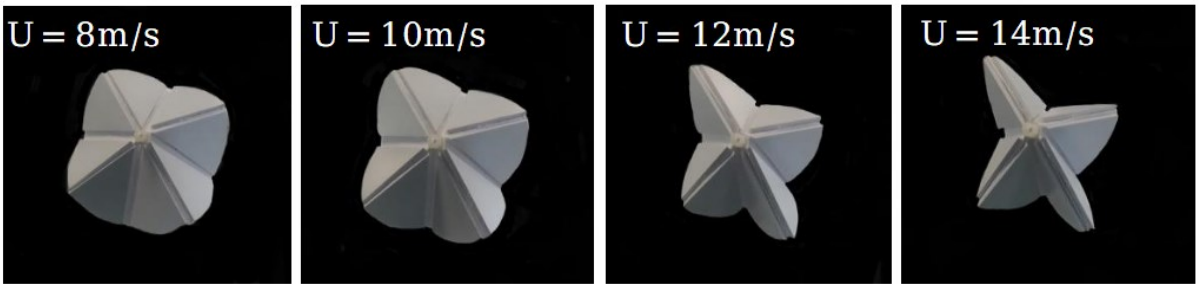

Figure 11: examples of 8-creases configurations' folding at varying wind speed: U=8m/s, 10m/s, 12m/s, and 14m/s, respectively

At each stage of the deformation, the cell's frontal area (the projected area in the frontal plane) changes. dentifying this area is crucial, as it acts as a pivotal parameter in our discussions on the Reynolds number, the Cauchy number, pressure drag as well as skin drag, and can be achieved by geometrically relating the space angles and the radius of the cell (identified in the figure at the top of the section) with trigonometry. The degree of closure is captured by a sport camera fixed at the front (inside the wind tunnel) and a recording device at the side (outside the wind tunnel). Observation on the single DOF folding shows good agreement with the previous assumption, and matched our common sense: greater the wind speed, higher the significance of deformation.

3.4. Experimental Results and Discussion

Typical results of the evolving deformation of bionic plates is reported in Figure, and the specimen set we discussed previously are shown as examples, denoted by the deformation angle-Cauchy number relationship. The difference among different crease numbers is also studied, in which we conclude: less significant closure is observed with plates with more creases, and the shape is corroborated by the theoretical model proposed in literature.

DOI: 10.54254/2753-8818/83/2025.20179

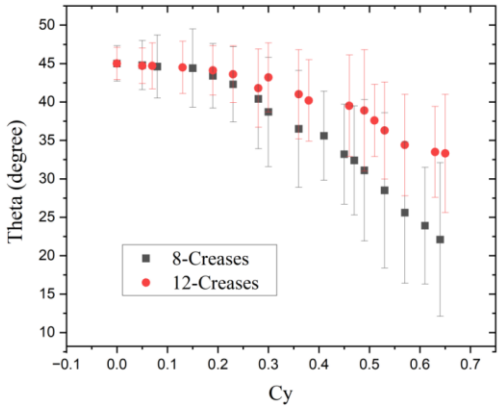

Figure 12: Deformation angle vs. Cauchy number graph for 8-crease plate and 12-crease plate. The error bars represent the standard deviation SD $= \sqrt{[\sum_{i=1}^{n}(x_i - \bar{x})^2]/(n-1)}$, calculated from the five data sets.

4. Computational Fluid Dynamics (CFD)

In this section, we use computational method to simulate unsteady 3-dimensional flow over the bionic plate. Assuming a fair degree of difference between the large time scale of the unsteady flow features and that of the genuine turbulence, the Reynolds-averaged Navier-Stokes (RANS) method is implemented here. The idea behind the equations is Reynolds decomposition, whereby an instantaneous quantity is decomposed into its time-averaged and fluctuating quantities, aiming to give approximate time-averaged solutions to the Navier-Stokes equations.

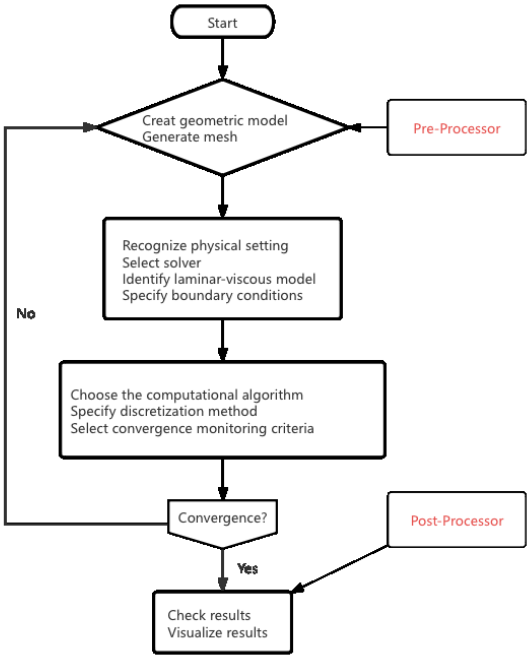

Figure 13: Procedure of CFD. In our context, we have implemented Second Order Upwind for spatial discretization.

DOI: 10.54254/2753-8818/83/2025.20179

4.1. Governing Equations

The continuity and momentum conservation equations for steady incompressible flow is written as:

$$\frac{\partial U_i U_j}{\partial x_j} = -\frac{1}{\rho}\frac{\partial \bar{P}}{\partial x_i} + \frac{\partial}{\partial x_j}(\nu \frac{\partial \overline{U_i}}{\partial x_j}) + \frac{\partial(-\overline{U'_i U'_j})}{\partial x_i x_j} \tag{17}$$

where U_i $(i = x, y, z)$ is the Reynolds-averaged velocity in tensor form (x_i is the Cartesian coordinate), P is the respective pressure, ν is the molecular kinematic viscosity, and $\overline{U'_i U'_j}$ is the resulted additional term -- Reynolds stress -- which is needed to be modeled:

$$-\overline{U'_i U'_j} = \upsilon_t(\frac{\partial U_i}{\partial x_j} + \frac{\partial U_j}{\partial x_i}) - \frac{2}{3}k\delta_{ij} \tag{18}$$

in which υ_t is the kinematic viscosity, and k and δ_{ij} are the turbulence kinetic energy (TKE) and the Kronecker delta, respectively. For the $k-\omega$ Shear Stress Transfer (SST) model we implement, the kinematic Eddy viscosity is written as:

$$\upsilon_T = \frac{a_1 k}{max(a_1\omega, SF_2)} \tag{19}$$

The turbulent kinetic energy is given:

$$\frac{\partial k}{\partial t} + U_j\frac{\partial k}{\partial x_j} = P_k - \beta^* k\omega + \frac{\partial}{\partial x_j}[(\nu + \sigma_k \nu_T)\frac{\partial k}{\partial x_j}] \tag{20}$$

The specific dissipation rate:

$$\frac{\partial \omega}{\partial t} + U_j\frac{\partial k}{\partial x_j} = \alpha S^2 - \beta\omega^2 + \frac{\partial}{\partial x_j}[(\nu + \sigma_\omega \nu_T)\frac{\partial k}{\partial x_j}] \tag{21}$$

And the closure coefficients are as follows:

$$F_2 = \tanh[[\max(\frac{2\sqrt{k}}{\beta^*\omega y}, \frac{500\nu}{y^2\omega})]^2] \tag{22}$$

$$P_k = \min(\tau_{ij}\frac{\partial U_i}{\partial x_j}, 10\beta^* k\omega) \tag{23}$$

$$F_1 = \tanh\{\{\min[\max(\frac{\sqrt{k}}{\beta^*\omega y}, \frac{500\nu}{y^2\omega}), \frac{4\sigma_{\omega 2}k}{CD_{k\omega}y^2}]\}^4\} \tag{24}$$

$$CD_{k\omega} = \max(2\rho\sigma_{\omega 2}\frac{1}{\omega}\frac{\partial k}{\partial x_i}\frac{\partial \omega}{\partial x_i}, 10^{-10}) \tag{25}$$

$$\phi = \phi_1 F_1 + \phi_2(1 - F_1) \tag{26}$$

$$\alpha_1 = \frac{5}{9}, \alpha_2 = 0.44) \tag{27}$$

$$\beta_1 = \frac{3}{40}, \beta_2 = 0.0828 \tag{28}$$

$$\beta^* = \frac{9}{100} \tag{29}$$

$$\sigma_{k1} = 0.85, \sigma_{k2} = 1 \tag{30}$$

$$\sigma_{\omega 1} = 0.5, \sigma_{\omega 2} = 0.856 \tag{31}$$

4.2. Computational Domain and Boundary Conditions

The plate's geometric center is defined as the origin of the Cartesian coordinate, in which x, y, z stand for the streamwise, cross-flow and spanwise orientations. A uniform streamwise velocity U is

DOI: 10.54254/2753-8818/83/2025.20179

specified at the inlet. The Reynolds number based on U and the equivalent diameter of the geometry D_e is given as:

$$Re = \frac{UD_e}{\nu} \tag{32}$$

A Neumann boundary condition for the velocity is specified at the downstream outlet, along with a Dirichlet condition for the pressure. We impose a free-slip boundary on the four sides of the computational domain, and a non-slip boundary on the surface of the 8(12)-slice configuration. The computational domain is discretized into a grid of approximately 3.8×10^6 hexahedral elements, and the mean drag and lift coefficients have been checked for mesh convergence.

Force is characterized by its three components along the coordinate directions: F_x, F_y, F_z, which can be calculated integrating pressure and viscous stresses acted on the plate surfaces. In our situation, F_x represents the drag force for which we are the most interested to solve, and F_y, F_z are the lift forces in the y and z directions, respectively. The corresponding non-dimensional force coefficients are denoted by

For SKE, the values of constants are given as follows:

$$C_d = \frac{F_d}{\frac{1}{2}\rho U^2 \frac{\pi}{4} {D_e}^2}, C_y = \frac{F_y}{\frac{1}{2}\rho U^2 \frac{\pi}{4} {D_e}^2}, C_z = \frac{F_z}{\frac{1}{2}\rho U^2 \frac{\pi}{4} {D_e}^2} \tag{33}$$

giving the magnitude of the coefficient of lift:

$$C_l = \sqrt{{F_y}^2 + {F_z}^2} \tag{34}$$

4.3. Simulation Parameters and Procedure

We use Ansys Fluent, a computational fluid dynamics computer code developed and marketed by Fluent Inc., as the platform for our simulation. The code implements a cell-centered finite-volume method: first, we create a geometry that gives Fluent the physical domain to work on -- that is, the configuration we drew to resemble a leaf; then, the domain is divided into small discrete control volumes (in other words, cells) by a pre-processor code that creates a computational mesh (in our context, the meshing software used is Fluent Meshing); once the domain is meshed, the integral forms of the governing equations are applied to the control volumes, and a set of non-linear algebraic equations for the discrete dependent variables are created, which are then linearised using an implicit method. Doing so produces a set of scalar equations, which include only 1 equation per computational control volume per DOF. To solve this resultant scalar equation system, a Gauss-Siedel linear equation solver and an algebraic multigrid (AMG) method are used in conjunction. Furthermore, because the equations are non-linear, several iterations of solution must be performed before we obtain a converged one.

Once the solution successfully converges and a desired level of accuracy is reached (by adjusting the fineness of mesh), we can move on to the pressure-velocity coupling. The governing equations -- including the momentum equation and the continuity equation -- are solved. However, for each cell the three components of velocities calculated using the sequential system may not satisfy the continuity equation, thus a Poisson-type equation is derived and then solved to obtain necessary corrections to the pressures and velocities. Note that these component momentum equations are solve in a way that the velocity components relevant to pressure are seen as unknown variables, meaning that these equations are used as functions of pressure, while pressure is not an explicit term in the continuity equation for incompressible flows. Aiming to introduce pressure into the equation, Fluent provides the Semi-Implicit Method for Pressure-Linked Equations (known as SIMPLE) algorithm to achieve this, which we implement in our calculation process.

DOI: 10.54254/2753-8818/83/2025.20179

SIMPLE algorithm basically implements a relation between velocity and pressure corrections to enforce mass conservation and obtain the pressure distribution. A variation of the SIMPLE algorithm, the SIMPLE-C (SIMPLE-Consistent) algorithm expresses the variable flux through each face of the cell in a more refined way. Furthermore, the Pressure-Implicit with Splitting of Operators (or the PISO pressure-velocity coupling scheme), another part of the SIMPLE algorithms family, takes root on higher approximation for the correlation between pressure and velocity corrections. Although the CPU time taken to run one solver iteration using the PISO algorithm is longer, the number of iterations needed to obtain a convergent result can be dramatically decreased thanks to the PISO.

Turbulent flows are defined by rapidly changing velocity fields that vary significantly across both space and time. Due to the wide range of scales at which these fluctuations occur, directly simulating both the small-scale and high-frequency variations is demanding: it requires an extremely fine computational grid. To eliminate the need to resolve the small scales, we implement the RANS method (Reynolds Averaging) that we've introduced earlier. In this approach, all flow variables are divided into a slowly varying component and a swiftly fluctuating one. Then, all equations are time-averaged to remove the rapidly fluctuating component. In Navier-Stokes equations, new terms are generated through this process, and these terms are known as the Reynolds stresses also given in the first section.

4.4. Simulation Results and Discussion

This section of study focuses on simulating the aerodynamic situation of the uniform flow passing the bionic foldable plate. The Reynolds-averaged pressure on the 8-crease cell is distributed as shown in FIGURE 14.(a), suggesting that pressure is negatively correlated with distance to the cell center. The turbulent energy on the back of the plate is shown in FIGURE 12.(b), from which we notice that the highest TKE values are concentrated near the top edge of the plate, indicated by the red and orange regions that result from a separation of the flow and the cortex shedding. FIGURE 14.(c) presents the velocity distribution. Some areas experience flow separation and wake formation, leading to sharp decrease in velocity in these regions. The highest velocity regions are in front of and around the sides of the plate, represented by the red and yellow regions.

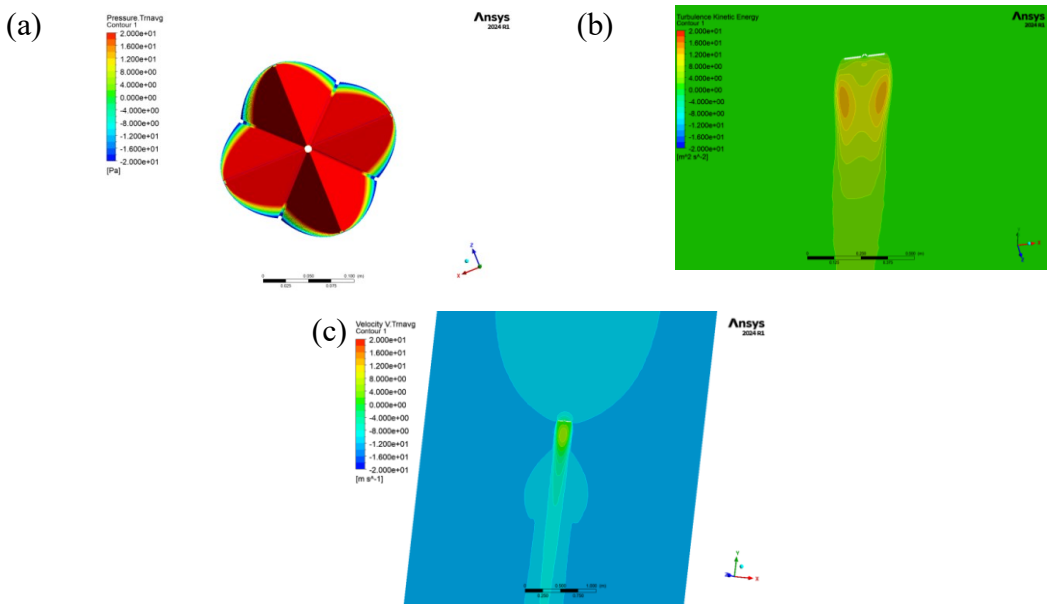

Figure 14: On the 8-crease configuration, contour plots of (a) Reynolds-averaged Pressure distribution on the plate's surfaces; (b) turbulent kinematic energy; (c) Averaged velocity.

DOI: 10.54254/2753-8818/83/2025.20179

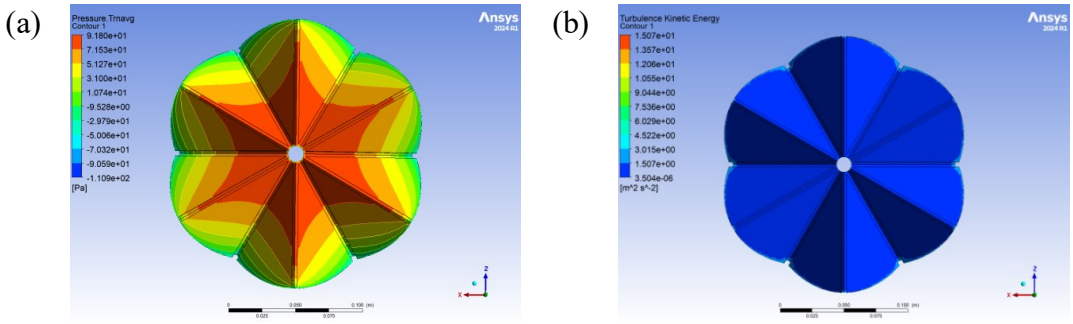

Figure 15: On the 12-crease configuration, contour plots of (a) averaged pressure distribution; (b) turbulent kinematic energy.

For the planar plate with 12 creases, the trend of change in aerodynamic parameters shows good agreement with that of the 8-crease ones. However, it is more apparent on the 12-crease configuration that the turbulent kinematic energy is slightly higher at the margin, which again emphasizes the existence of a wake.

5. Concluding Remarks and Outlooks

The deformation mechanism and mechanical response of leaf-resembled foldable plate is studied and simulated. We constructed a 2-D conical theoretical model where we study the velocity and pressure distribution from its energy and drag force characteristics -- specifically, the dynamic balance between fluid-induced and elastic torques acted on a two-dimensional foldable plate with rigid panels connected by a hinge with torsional stiffness. By implementing the governing equations of fluid dynamics, including the continuity equation and the momentum equation, we have obtained the pressure-induced drag as a function of the ratio of effects of inertia force and elastic force (known as the Cauchy number, C_y), and its relation with the deformation, characterized by the fold angle θ, is as well explored. Furthermore, we implement the Falkner-Skan method to incorporate shear stress into the discussion, and gained numerical solution to this second-order ODE.

We test the deformation angle as a function of Cauchy number, which reveals good correspondence with the theoretical model. Prior of that, several parameters are thoroughly measured and calculated -- including the geometrical constants and the range of Reynolds number. However, the lift force applied on the plates is a few order of magnitudes smaller than the scale of the dynamometer when measuring the fold stiffness, κ, as well as the drag exerted on the planes by wind, making the measurement significantly diverged from expectation. In future study, we hope to ameliorate experimental methodology in order to obtain drag values for varying Cauchy number, and more accurate fold stiffness data.

Furthermore, to visualize the aerodynamic situation anticipated by our theoretical model, CFD on a semi-folded configuration is performed, which no only agrees with the pressure and velocity distribution we yield from drag and energy analysis, but also gives insights into the wake formation which we have not discussed theoretically. Inspired by the CFD result, we feel deeply impulsed to continue replenishing theoretical discussion from a broader range of perspectives: from the velocity distribution at the boundary layer, to the formation of wake at the back of the plane; from plates with 8 and 12 folds, to a wider range of fold numbers (plausibly odd numbers that do not satisfy symmetry); from radially symmetrical leaf model, to more commonly observed simple leaf structure -- anyhow, steps to consummation are infinite, and we with infinite curiosity shall hold on to render this study give rise to further applications.

DOI: 10.54254/2753-8818/83/2025.20179

References

[1] *Marzin T, de Langre E, Ramananarivo S. (2022) Shape reconfiguration through origami folding sets an upper limit on drag.*
[2] *V. Brunck,1 F. Lechenault, A. Reid, and M. Adda-Bedia (2016) Elastic theory of origami-based metamaterials*
[3] *Lionel Schouveiler and Christophe Eloy (2020) Flow-Induced Draping*
[4] *H.Kobayashi, B.Kresling and J. F. V. Vincent (1998) The geometry of unfolding tree leaves*
[5] *Yuxin Wu, Jianzhi Yang, Helge I. Andersson, JianYu Chen, and Xiaowei Zhu (2024) On the transitional wake past a streamwise rotating prolate spheroid*
[6] *Brennen. Caltech Falkner-Skan Solutions to Laminar Boundary Layer Equations*
[7] *University of Illinois Urbana-Champaign Lecture 7. Falkner-Skan Solutions*
[8] *Zhengtong Xie and Ian P Castro (2006) LES and RANS for Turbulent Flow over Arrays of Wall Mounted Obstacles*
[9] *D.A. Jones, D.B. Clarke (2008) Simulation of Flow Past a Sphere using the Fluent Code*